Micro-structured medium with large isotropic negative thermal expansion

Luigi Cabras[1], Michele Brun[2] and Diego Misseroni[3]

[1]Dipartimento di Ingegneria Meccanica e Industriale, Universitá di Brescia, via Branze 38, Brescia, 25123, Italy
[2]Dipartimento di Ingegneria Meccanica, Chimica e dei Materiali, Universitá di Cagliari, via Marengo 2, Cagliari, 09123, Italy
[3]Dipartimento di Ingegneria Civile, Ambientale e Meccanica, Universitá di Trento, via Mesiano 77, 38123 Trento, Italy

MB, 0000-0002-4760-9062

A challenge in nano- and micro-mechanics is the realization of innovative materials exploiting auxetic behaviour to tailor thermal expansion properties. For this purpose, a new class of micro-structured media possessing an extremely wide range of tunable (positive, negative or even zero) thermal expansion is proposed and analytically and experimentally assessed. For this class of isotropic *Mechanical-Auxetic Thermal-Shrinking* media, the effective coefficient of thermal expansion is explicitly linked to two microstructural variables via a simple relation, allowing the design with desired values. The theoretical predictions for the negative thermal properties are fully validated by the experimental and numerical outcomes. The simplicity of the proposed structure makes the design useful for the production of a new generation of advanced media, with applications ranging from micromechanical devices to large civil and space structures.

Subject Areas:
mechanical engineering, mechanics, structural engineering

Keywords:
negative thermal expansion, mechanical-auxetic thermal-shrinking, micro-structured medium, architected materials, Poisson's ratio

Author for correspondence:
Michele Brun
e-mail: mbrun@unica.it

1. Introduction

The coefficient of thermal expansion (CTE) is the measure of the deformation suffered by a material loaded by a unitary change of temperature. Normally, a body expands upon heating and contracts upon cooling (positive CTE); however, there exist natural and engineered systems, which have the capability to shrink upon heating, showing a negative CTE. The new design reported in figures 1 and 2 gives the possibility to tune the CTE in a wide interval, ranging from positive to negative values.

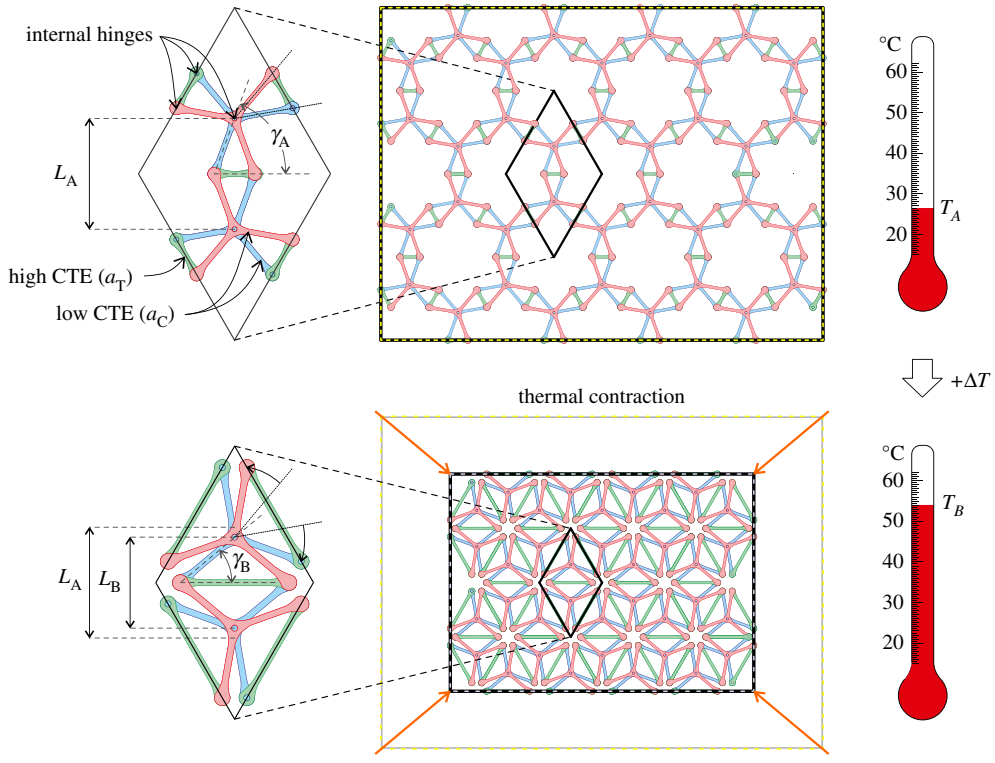

Figure 1. Microstructure of the *Mechanical-Auxetic Thermal-Shrinking* (MATS) medium. Low CTE Y-shaped elements are coupled with high CTE longitudinal elements. As a result of an applied thermal gradient ΔT, thermal expansion of the single phases is counterbalanced by the internal relative rotation of the Y-shaped elements resulting in a macroscopic contraction. (Online version in colour.)

The capacity to control thermal expansion is a key factor that directly affects structural safety in large-scale structures subjected to severe temperature variations such as bridges, aircraft, space structures, piping systems, industrial machineries and energy plants. In these systems, a low or even zero CTE reduces thermal stresses and improves dimensional stability; it also mitigates the effects of thermal shocks in Pyrex® glass. Strict control of thermal deformation is necessary in precision optical instruments; for instance a minute error in the positional accuracy between the primary and vice fillings in astronomical optics telescopes dramatically reduces the aperture efficiency of Q-band observations [1]. In such structures, the capability to control both thermal and mechanical deformations is of primary importance [2–4]. Dental fillings in biomedical applications need to have their expansion coefficients matched to those of teeth [5] and negative thermal expansion (NTE) can be used to lower the overall expansion coefficient of a composite to obtain a predetermined value. By contrast, materials with extremely large expansion are employed as thermal actuators [6], while NTE and Poisson's ratio can also be implemented in MEMS to reduce fatigue problems under in-service thermal cycling [7]. It is then clear that a medium that can be easily designed to have a predetermined CTE in a broad range of temperature working conditions is extremely attractive in different technological applications.

NTE was obtained in few synthetized materials; cubic zirconium tungstate (α-ZrW_2O_8) was shown to contract continuously and isotropically upon heating within a broad range of temperatures [8,9]. Mixed oxides ZrP_2O_7 and $Sc_2(WO_4)_3$ families display NTE [10], as well as some glasses belonging to the titania–silica family [11] at room temperature and silicon and germanium [12] at very low temperatures ($< -170°C$). However, the use of these materials is

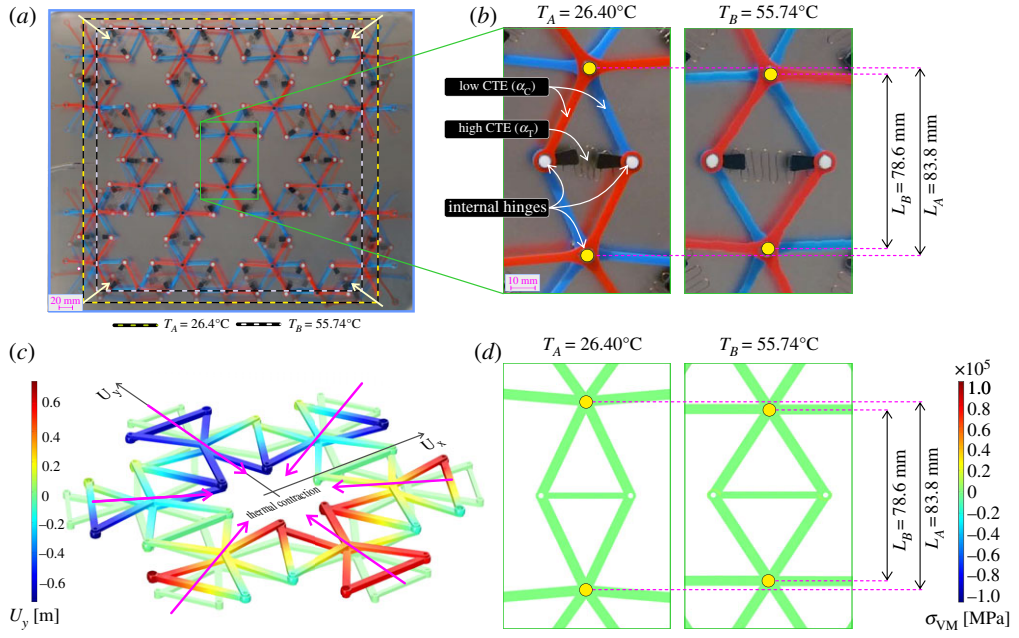

Figure 2. Experimental and numerical results. (*a*) Superposition of snapshots taken at temperatures $T_A = 26.40^\circ$C and $T_B = 55.74^\circ$C. (*b*) Detail of the initial and final configurations of the central cell of the micro-structured medium. (*c*) 3D finite-element simulations in Comsol Multiphysics with the detail of one cell (*d*). Contour plots show (*c*) displacement and (*d*) Von Mises stress. (Online version in colour.)

limited by the durability and robustness requests over large temperature intervals. Alternatively, architected micro-structured media have been shown to provide thermal properties that cannot be achieved by other materials. They are designed to release thermal deformation through internal mechanical mechanisms, they can be made of conventional materials and they are scale-invariants when the internal structure has a typical size greater than 10^{-1} µm. The effective CTE is governed by the microstructure and the contrast between the CTEs of the constituents.

Periodic lattice models are found to give unprecedented CTEs, they were first proposed by Lakes *et al.* [13–15] and theoretical models of triangular lattices have been shown to give adjustable thermal expansion in 2D [16–18] and in 3D [17,19]. NTE lattices are lightweight-structured media with good mechanical properties that can be used in satellites for support of appendages such as antennae and photovoltaic arrays [20], but also as thin film of 1 µm thickness with unit cell size of 102 µm to be integrated in thermally stable space telescope mirrors [21,22]. These architected media provide better performance than multiphase composites such as laminates [23–25] and particulates with needle-like inclusions [26]. Due to the internal architecture, they easily give omnidirectional isotropic CTE. They can also combine NTE and negative Poisson's ratio [27,28] and expand or contract when actuated by either external temperature or mechanical fields as in the recently proposed tunable *in situ* 'origami metamaterial' [5]. Such MATS-structured media incorporate tailorable CTEs and tunable Poisson's ratios with advanced integration of multi-functions [29]. The main limitations of NTE lattices concern possible thermal fatigue issues, since thermal cycles induce non-negligible thermal stresses in such slender micro-structured media, a problem that is practically absent in the proposed model. Here we combine theoretical analysis and experimental validation to show a novel lattice structure that exhibits the capacity to be tailored to a specific value of the CTE (positive, negative or even zero). Strongly negative, null or positive CTEs are achieved using conventional constituent materials with positive CTEs, in particular the experimental

results reveal an effective negative CTE $\alpha_E \approx -2 \times 10^3$ μm/(m°C). The micro-structured medium integrates high thermal performances with the simplicity of the design, since the effective CTE α_E in equation (2.1) depends only on two internal variables: the contrast ratio between the constituents' CTEs and a single topological parameter. The internal architecture has been designed to remove internal kinematical constraints; in the structural mechanics terminology, it is called a statically determined structure. Therefore, as we show in figure 2*d*, it can release thermal deformations without developing internal mechanical stresses drastically reducing problems of thermal fatigue. The MATS lattice can simultaneously combine NTE and negative Poisson's ratio (arbitrarily close to the thermodynamic limit value −1 [30]). The effective CTE and Poisson's ratio can be designed independently by varying the contrast of the CTEs and the longitudinal stiffness between the ligaments and the arms of the cross-shaped elements. The effective behaviour is thermally and mechanically isotropic and, if needed for special applications, it can be easily made anisotropic by varying the thermo-mechanical constitutive properties of a single or a couple of ligaments within the unit-cell.

The paper is organized as follows. In §2, we describe the internal microstructure of the auxetic lattice, while the effective CTE is derived in §3. Details of the experimental set-up are reported in §4, the post-processing analysis of the experimental data is given in §5, followed by a comparison with numerical and analytical results in §6.

2. The micro-structured medium

We begin from the topology reported in [30] to design a unit structure capable of volumetric contraction with increasing temperature. The unit shown in the left of figure 1 represents the basic building block used to construct the periodic medium with a negative CTE. The single unit is composed of two Y-shaped elements with a positive CTE α_C, linked together by longitudinal elements with a positive CTE α_T . At the centres and the ends of the Y-shaped elements internal hinges allow relative rotations and prevent relative displacements. The effective CTE derives from the combined effect of the thermal expansion of each structural element and the internal rigid-body mechanism induced by the mismatch $\alpha_T - \alpha_C$. The internal mechanism is responsible for the macroscopic thermal contraction.

The effective CTE is given by the simple relation

$$\alpha_E = \frac{(1 - \eta \cos^2 \gamma)}{\sin^2 \gamma} \alpha_C, \tag{2.1}$$

where the contrast ratio is $\eta = \alpha_T/\alpha_C$ and the angle γ describes the configuration of the microstructure. In the range $\eta > 1/\cos^2 \gamma$, the effective CTE is negative, as reported in figure 3*b*.

3. Effective coefficient of thermal expansion

The analytical expression of the effective CTE is determined as follows. We draw from the lattice the triangle shown in figure 4. The point 3 represents the centre of the Y-shaped elements visualized in blue and red in figure 1 of the main article, whereas the spring elements are represented by the green line connecting nodes 1 and 2. The vertical displacement of the point 3 identifies the effective thermal deformation; its magnitude for a change of temperature ΔT, depends on the thermal deformation of the cross-shaped and longitudinal elements. This vertical displacement can be computed as the sum of two contributions, the displacement for $\alpha_C \neq 0$ and $\alpha_T = 0$ plus the displacement for $\alpha_C = 0$ and $\alpha_T \neq 0$, as shown in figure 4:

$$L_1 - L_0 \simeq \frac{p\, \alpha_C\, \Delta T}{\sin \gamma} - \frac{p\, \alpha_T\, \cos^2 \gamma\, \Delta T}{\sin \gamma}, \tag{3.1}$$

where $\Delta T = T - T_0$, T_0 being the initial and T the actual temperature. Formula (3.1) is a linearization in ΔT and γ should be intended as $\gamma_0 = \gamma(T_0)$ there. The exact expression, nonlinear

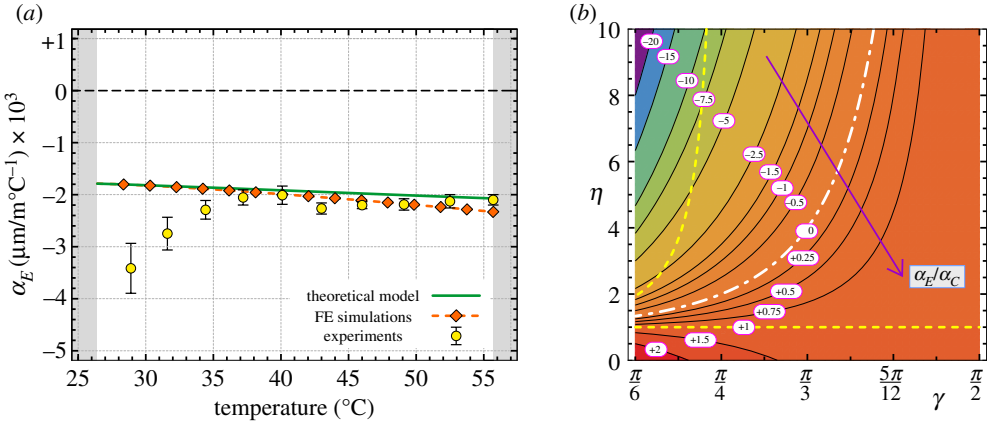

Figure 3. (*a*) Effective CTE α_E as a function of the temperature T in the interval $T_A \leq T \leq T_B$. The analytical values are indicated with a green line, the numerical ones with a red dashed line with diamonds and the experimental ones with yellow dots. Error bars indicate standard deviation of the data for six different experiments. (*b*) Relative CTE ratio α_E/α_C as a function of the CTE ratio $\eta = \alpha_T/\alpha_C$ and of the geometrical parameter γ. The white dash-dotted line indicates the transition between positive and negative effective CTE α_E. The yellow dashed lines separate the parametric regions where $|\alpha_E| \gtrless \max(\alpha_C, \alpha_T)$. Contour labels indicate the values of the ratio α_E/α_C. (Online version in colour.)

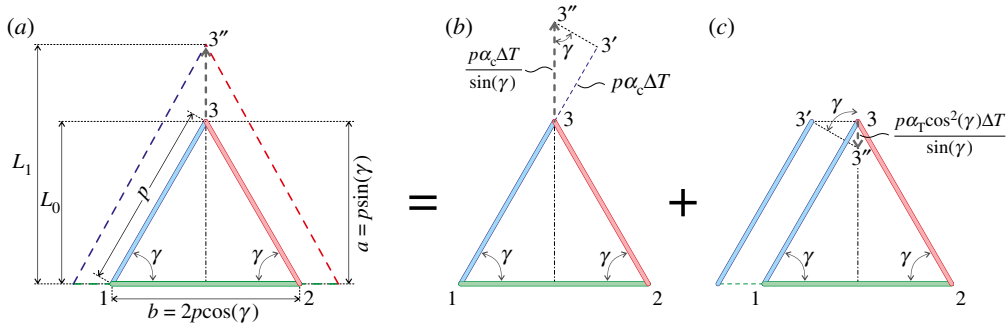

Figure 4. Analytical computation of the linear CTE. The height variation $L_1 - L_0$ of the triangle 123 due to a temperature change ΔT (*a*) is the sum of the displacement of the point 3 for $\alpha_C \neq 0$ and $\alpha_T = 0$ (*b*) and the displacement of the point 3 for $\alpha_C = 0$ and $\alpha_T \neq 0$ (*c*). (Online version in colour.)

in ΔT, is

$$L_1 - L_0 = p\left[\sqrt{(1+\alpha_C\,\Delta T)^2 + (1+\alpha_T\,\Delta T)^2\cos^2\gamma_0} - \sin(\gamma_0)\right]. \tag{3.2}$$

The effective CTE is

$$\alpha_E = \frac{L_1 - L_0}{L_0}\frac{1}{\Delta T} = \frac{(1-\eta\cos^2\gamma)p\alpha_C\Delta T}{\sin\gamma}\frac{1}{p\sin\gamma}\frac{1}{\Delta T}, \tag{3.3}$$

which is equal to expression (2.1). We note that it is possible to consider definitions of deformation different from the Cauchy or engineering strain $(L - L_0)/L_0$, such as the logarithmic or true strain $\log(L/L_0)$ or the Green–Lagrange strain $(L^2 - L_0^2)/(2L_0^2)$. Such measures give different values in the nonlinear range, but they all linearize to expression (2.1). We also note that nonlinear effects result from the dependence of the phase thermal coefficients α_T and α_C on the temperature T and to the geometric nonlinearity, associated with the evolution of the microstructure, which is described by the variation of the parameter γ. In such a case, the value of the effective coefficient of the thermal

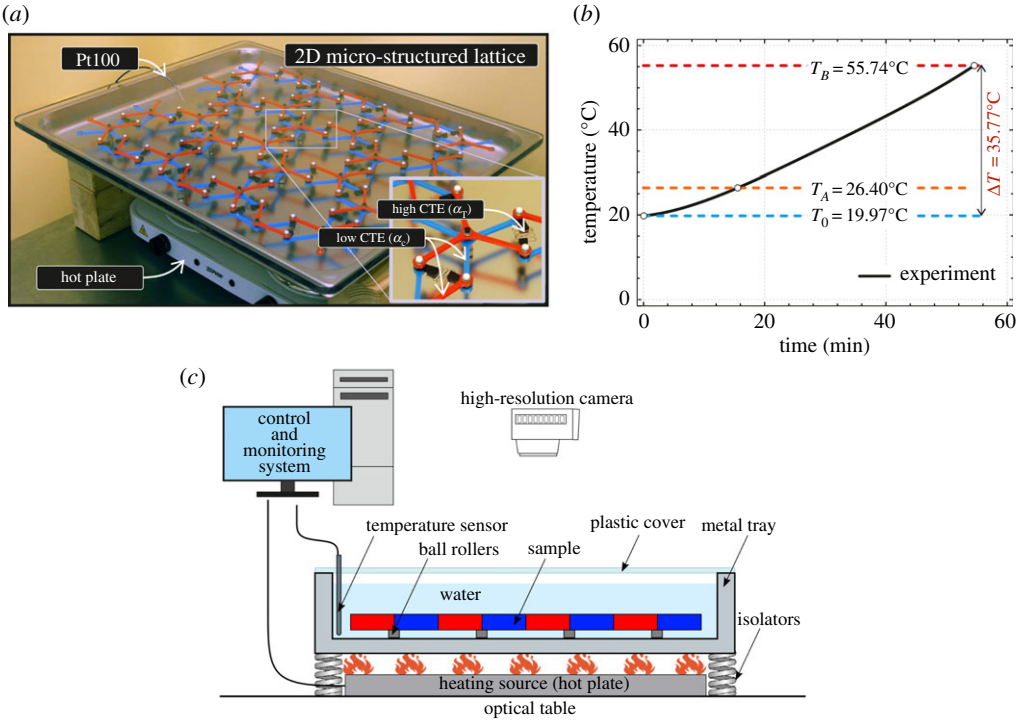

Figure 5. Experimental set-up. (*a*) The 2D lattice is placed in the metal tray and covered with the transparent plastic cover. The hot plate is the heat source, while the temperature is monitored by the resistance detector PT100. (*b*) Imposed time evolution of the temperature for the experimental environment. (*c*) Scheme of the experimental set-up. (Online version in colour.)

expansion depends on the initial temperature T_0 and configuration, described by $\gamma_0 = \gamma(T_0)$ and $L_0 = L(T_0)$.

In the linearized regime, α_E/α_C is a point in the (η, γ)-space. When nonlinear geometric effects are considered, they are described by the evolution of γ with the temperature and correspond to a straight line at $\eta = \text{const.}$ in the (η, γ)-space. At increasing temperature, the angle γ decreases when $\eta > 1/\cos^2\gamma$ ($\alpha_E < 0$) and increases when $\eta < 1$ ($\alpha_E > 0$), increasing the magnitude of α_E, either negative or positive. A dependence of the CTEs α_T and/or α_C on the temperature will lead to a continuous curve in the (η, γ)-space and in such a case it is in principle possible to switch from positive to negative CTE and vice versa, as a result of the dependence of η on the temperature.

4. Experimental set-up

The negative effective CTE α_E was verified experimentally; the experiments were performed at the 'Instabilities Lab' of the University of Trento. In figure 5*a*, it is possible to see in detail the experimental set-up and the geometrical properties of the lattice, while a schematic model is reported in figure 5*c*. The Y-shaped elements and the ligaments connecting the ends of the arms are made up of two different materials, both with positive coefficients of thermal expansion α_C and α_T (figure 5*a*). The Y-shaped elements were milled, using an EGX-600 engraving machine (Roland), from 4 mm thick sheets of PMMA (Perspex® blue 727 and red 431 distributed by Bayer AG), with Young's modulus $E = 3350$ MPa, Poisson's ratio $\nu = 0.35$ and glass transition temperature $T_g = 105$°C. The polymeric material has the low CTE $\alpha_C \approx 70\,\mu\text{m}/(\text{m}^\circ\text{C})$, in the temperature range 19.97–55.74°C.

The flat springs, connecting the Y-shaped elements, are made of Nitinol (NiTiCu) shape memory alloy and were purchased from Kellogg's Research Lab, USA. Such springs have

diameter 0.5 mm, length 50 mm, amplitude 20 mm, pitch 20 mm and transition from martensitic to austenitic structure in the temperature range 35–55°C (see also figure 2*b*). They were adopted to amplify the thermal expansion effect at the macroscale and to reach large thermal displacements of around 10^{-2} m. The large CTE α_T was estimated using two independent procedures. First, by clamping a set of five springs at one end and applying an increasing thermal load from 15°C to 60°C; the resulting thermal elongations where then measured to give $\alpha_T = 8022 \pm 173$ μm/(m°C). Second, α_T was estimated by an inverse approach comparing the effective thermal contraction measured in the actual experiment shown in figures 2*a*,*b*, with the results of a parametric finite-element simulation performed in Comsol Multiphysics (figure 2*c*,*d*).

The blue and red elements were hinged at their centre with two rolling bearings (from MISUMI Europa GmbH) to reduce the rotational friction; one hinge couples the red and the blue Y-shaped elements in their centre, whereas other hinges are placed at the end of each arm to join the different Y-shaped elements and the shape memory alloys' springs. They are visible in black and white, respectively, in figure 2*b*.

The structure was placed in a metal tray, where it was free to expand; it was then covered with water. As shown in figure 5*c*, the sample is subjected to free boundary conditions in the plane of expansion. In order to minimize the effect of friction, the contact between the structure and the tray was obtained using six ball rollers (from MISUMI Europa GmbH). The system was subjected to a change of external temperature in a controlled environment. A transparent plastic cover was used to reduce temperature gradients over the whole structure. The source of heat was a hot plate controlled by a rugged and reconfigurable control and monitoring system (NI CompactRIO), interfaced with a system-design platform commonly used for data acquisition and instrument control (Labview 2018-National Instruments). The temperature was simultaneously measured with a resistance temperature sensor (PT100). The temperature of the environment was then increased gradually from $T_0 = 19.97$°C to $T_B = 55.74$°C in a time interval of 55 min, as shown in figure 5*b*. The model was mounted on an optical table (made by Technical Manufacturing Corporation) and equipped with four Gimbal Piston™ air isolators to prevent spurious vibrations. The table was also monitored for vibrations using integrated electronic piezoelectric (IEPE) accelerometers (PCB Piezotronics Inc., model 333B50).

The thermal displacements were recorded with a high-resolution camera (Sony Camcorder HDR-XR550) and a movie was recorded with a Sony camcorder (model HDR-XR550). Circular markers were placed at the centres of the Y-shaped elements; at these points, the local and the macroscopic displacements coincide.

5. Analysis of experimental results

At each temperature T_i, the positions of nodal points were tracked frame by frame by digital image correlation (figure 6*a*), using an algorithm implemented in Matlab [30]. The CTE at temperature T_i for the nodal point j is

$$\alpha_{E,j}(T_i) = \frac{\varepsilon_{T,j}(T_i)}{T_i - T_A} = \frac{1}{T_i - T_A}\frac{L_j(T_i) - L_j(T_A)}{L_j(T_A)}, \tag{5.1}$$

where $L_j(T_i)$ is the distance of the point j from the centre of mass of all nodal points at temperature T_i and $T_A = 26.4$°C. The temperature interval $[T_A, T_B]$ has been subdivided into $N_T = 11$ steps, the initial temperature $T_A = 26.4$°C was chosen to avoid the initial thermo-mechanical adjustment of the system. At each step, the centre of mass is $\underline{X}_0(T_i) = \sum_{j=1}^{N_P} \underline{X}_j(T_i)/N_P$, where $N_P = 22$ is the number of tracked nodal points and $\underline{X}_j(T_i)$ their positions at temperature T_i. The distance is $L_j(T_i) = |\underline{X}_j(T_i) - \underline{X}_0(T_i)|$. The thermal deformations $\varepsilon_{T,j}(T_i)$ in each nodal point j at each temperature T_i are shown in figure 6*b* in red dots connected by continuous lines.

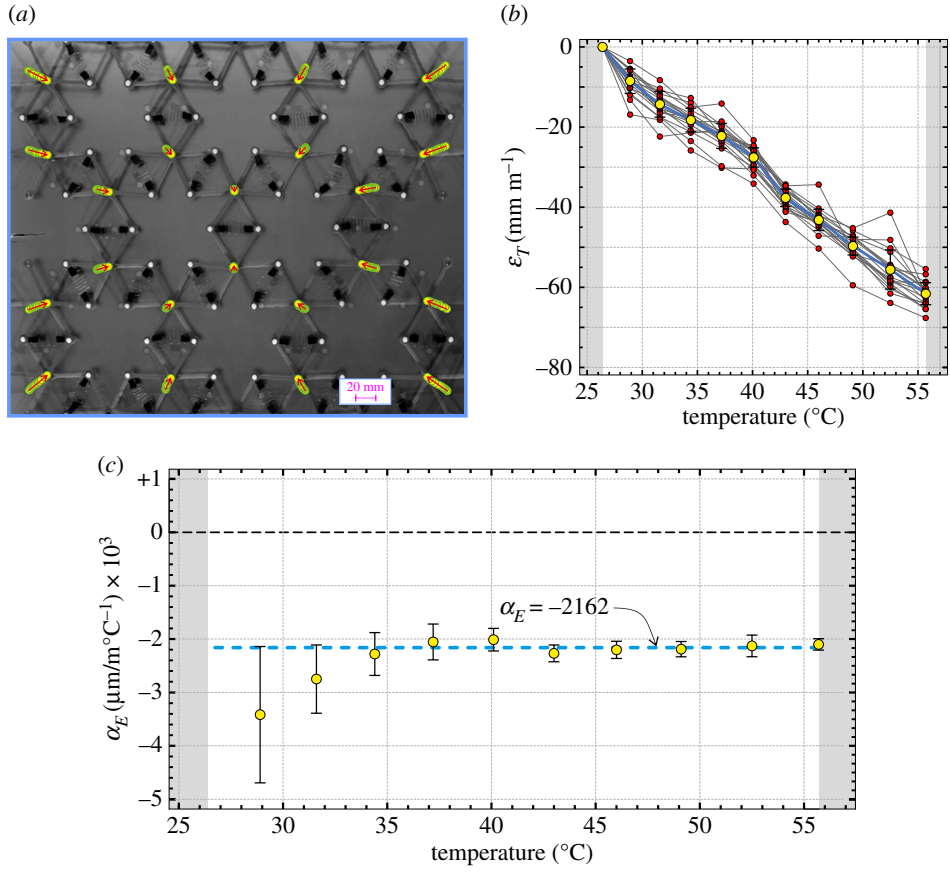

Figure 6. (*a*) Tracking of the position of nodal points in the temperature interval $T_A = 26.40^\circ\text{C} \leq T \leq T_B = 55.74^\circ\text{C}$. Yellow dots indicate the evolution of the position of the 22 tracked points, while red arrows indicate their total displacement from the configuration at T_A to the configuration at T_B. (*b*) The thermal deformations of nodal points as a function of the applied temperatures T_i ($i = 0, \ldots, 10$). Red and yellow dots indicate the thermal deformations $\varepsilon_{T,j}$ and their sample mean $\overline{\varepsilon}_T$. (*c*) Effective CTE α_E in the temperature interval $T_A \leq T \leq T_B$. The effective CTE α_E is indicated with a blue dashed line, the sample means $\overline{\alpha}_E(T_i)$ of the CTEs are indicated with yellow dots. Sample standard deviations $\sigma(T_i)$ are also shown as error bars. (Online version in colour.)

The sample mean of $\alpha_{E,j}(T_i)$ at any temperature T_i is

$$\overline{\alpha}_E(T_i) = \frac{\overline{\varepsilon}_T(T_i)}{T_i - T_A} = \frac{1}{T_i - T_A} \sum_{j=1}^{N_P} \frac{\varepsilon_{T,j}(T_i)}{N_P}, \tag{5.2}$$

where the sample means of the thermal deformations $\overline{\varepsilon}_T(T_i)$ at each temperature T_i are shown in figure 6*b*, while $\overline{\alpha}_E(T_i)$ are reported in figure 6*c*.

The sample standard deviation of $\overline{\alpha}_E(T_i)$, also indicated in figure 6*c*, is given by

$$\sigma(T_i) = \sqrt{\frac{\sum_{j=1}^{N_P} \left(\alpha_{E,j}(T_i) - \overline{\alpha}_E(T_i)\right)^2}{N_P - 1}}, \tag{5.3}$$

while the standard error of the sample mean is

$$\delta(T_i) = \frac{\sigma(T_i)}{\sqrt{N_P}}. \tag{5.4}$$

The CTE $\alpha_E(T_i)$ at any temperature T_i is $\alpha_E(T_i) = \overline{\alpha}_E(T_i) \pm \delta(T_i)$, this is the effective CTE of the micro-structured medium at each temperature T_i. To evaluate the effective CTE averaged on the temperature range $[T_A, T_B]$, we have calculated the weighted mean of $\overline{\alpha}_E(T_i)$

$$\overline{\alpha}_E = \frac{\sum_{i=1}^{N_T} \omega_i \overline{\alpha}_E(T_i)}{\sum_{i=1}^{N_T} \omega_i}, \tag{5.5}$$

where the weights are $\omega_i = 1/\delta(T_i)^2$.

The error that is assigned to $\overline{\alpha}_E$ is obtained using the relation

$$\delta = \frac{1}{\sqrt{\sum_{i=1}^{N_T} \omega_i}}. \tag{5.6}$$

Finally, the effective CTE is

$$\alpha_E = \overline{\alpha}_E \pm \delta = -2162 \pm 20\ \mu\text{m}/(\text{m}^\circ\text{C}), \tag{5.7}$$

as shown in figure 6*c*.

6. Comparison with analytical and numerical results

The results of the experiment reported in figure 6*c* for the temperature increase from $T_A = 26.4^\circ$C to $T_B = 55.74^\circ$C verify the thermal contraction, thus showing a negative CTE α_E.

The effective CTE in the temperature interval $T \in [T_A, T_B] = [26.4^\circ\text{C}, 55.74^\circ\text{C}]$ has been estimated from the experimental data to be $\alpha_E \simeq -2162\ \mu\text{m}/(\text{m}^\circ\text{C}) < 0$. The experimental results, reported in figure 6*c*, also show that, for $T > 34^\circ$C, the effective CTE reaches a better defined value with oscillations of small amplitude and low standard deviation. The statistical analysis for the determination of the effective CTE α_E is supported by a movie of the numerical and experimental results. For $T < 34^\circ$, some springs display a fast martensitic to austenitic transition with large localized deformations. The relatively large local deformations cause in some cases lateral buckling of the springs and induce a larger magnitude of $\alpha_E < 0$. The localized deformations can be noted in the movie, which is available as electronic supplementary material.

In figure 2*a*,*b*, we report the superposition of the initial and final configurations at the initial temperature $T_A = 26.40^\circ$C and the final one $T_B = 55.74^\circ$C. The contraction due to thermal elongation is visible to the naked eye.

Additionally, figure 2*c*,*d* shows a finite-element numerical simulation of the experiment. A three-dimensional model composed of 107 051 tetrahedral elements was implemented in Comsol Multiphysics, where a single unit cell, representative of the behaviour of the periodic structure, was studied. In the simulation, we assumed the same material and geometrical properties as in the experiments for the Y-shaped elements; while the springs were approximated to prismatic bars with a rectangular cross section, the equivalent CTE $\alpha_T = 7984\ \mu\text{m}/(\text{m}^\circ\text{C})$ was determined by an inverse approach equating experimental and numerical displacements. Such a value is in good agreement with the value $\alpha_T = 8022 \pm 173\ \mu\text{m}/(\text{m}^\circ\text{C})$, detailed in §4, obtained from a set of five springs, constrained at one end and subjected to an increasing temperature from 15°C to 60°C. Internal hinges were added to constrain relative displacements between different parts of the numerical model. The numerical results, shown in figure 3, confirm the experimental findings, both qualitatively and quantitatively. The *thermal-shrinking* behaviour has been fully verified.

The comparison between experimental, analytical and numerical values of the effective CTE α_E, in the temperature interval $T_A \le T \le T_B$, is reported in figure 3*a*. The analytical CTE α_E, shown in a green continuous line, is computed by applying the first relation in equation (3.3), with the exact determination of the displacement, as in equation (3.2). The finite-element values, indicated by a red dashed line with diamonds, were computed by subdividing the temperature interval in 15 regular steps and performing a forward piecewise linear analysis where, at the end of each step, the configuration was updated by applying the computed thermal deformation. Again, the

thermal deformations were computed as $(L - L_0)/L_0$. Finally, experimental results are reported in yellow dots in Figure 3*a*. The experiment was repeated six times and error bars indicate standard deviation of the six test measures. The comparative analysis evidences the agreement between experimental, analytical and numerical results, confirming the negative CTE. The analytical and numerical curves show a variation of α_E with the temperature, which is associated with the evolution of the microstructure. In fact, the angle γ decreases monotonically from $\gamma(T_A) = 64^\circ$ to $\gamma(T_B) = 57.3^\circ$.

In figure 3*b*, the ratio α_E/α_C is reported as a function of the ratio $\eta = \alpha_T/\alpha_C$ and the angle γ, following the linearized expression (2.1). The results show the possibility to obtain positive, negative and zero values of α_E. The variation of the effective CTE as a function of η is more pronounced for smaller angles γ and it is maximized at the limiting value $\gamma = \pi/6$, where neighbouring crosses come into contact.

Interestingly, as also suggested by the dashed yellow lines in figure 3*b*, when $\eta < 1$, $\alpha_E > \alpha_C > \alpha_T$, so that the effective CTE is greater than the single phase values. In addition, when $\eta > 1/\cos(2\gamma)$, $|\alpha_E| = -\alpha_E > \alpha_T > \alpha_C$, showing the possibility to obtain an effective CTE α_E, which is negative and greater, in magnitude, than the phase coefficients α_C and α_T.

7. Conclusion

We have proposed the theory, the design and the experimental validation of a micro-structured medium with both negative CTE and negative Poisson's ratio. Such a micro-structured medium is denoted by *MATS*. In particular, (i) a closed-form equation is provided for the effective CTE α_E of the *MATS* as a function of two microstructural parameters; and (ii) an experimental campaign was performed to validate the theoretical model. The experimental results show a large NTE in agreement with numerical finite-element results and theoretical predictions.

The effective CTE can be easily tuned by varying the thermal expansion contrast ratio η between the two phases and the geometrical configuration of the internal structure, which can be described by the topological parameter γ. From figure 3*b*, it is evident that it is possible to reach highly negative, null or positive effective CTEs in a wide range, including magnitudes greater than the phase ones. Mechanical and thermal effects are coupled by the configurational parameter γ, but they can be varied independently by modulating the thermal contrast ratio η and the ratio between the longitudinal stiffnesses of the elements of the microstructure.

The design does not require materials with extreme properties, conventional materials being sufficient to get the desired thermal properties. Indeed, the effective CTE is not only an intrinsic property of the constituent materials, but it is correlated to the internal micro-structure.

Two fundamental features of the architected medium are the isotropy of the thermomechanical behaviour, which stems from the design of the microstructure, and the drastic reduction of internal thermal stresses, as revealed by the absence of stresses due to thermal contraction in figure 2*d*.

The insight gained by performing theoretical and numerical exploration serves as an important design guide for the future fabrication of practical micro-structured media for real-world applications. The overriding features of the above system are the simplicity of the model, the robustness of the behaviour and the magnitude of the effect. Each of these features points to a more practical method for producing NTE media, which can operate over a wide range of scales and temperature intervals.

Experimental results and numerical simulations are presented in the electronic supplementary material, a movie.

Data accessibility. Additional data concerning finite-element simulations (Comsol) and analytical derivation of the effective CTE (Mathematica) are provided as electronic supplementary material.

Authors' contributions. All the authors contributed to the development of the design, the analytical, numerical and experimental characterization and to the writing of the manuscript. D.M. had a leading role in the experimental part, L.C. in the numerical part and M.B. in the analytical part. All authors contributed equally to this study.

Competing interests. We declare we have no competing interests.
Funding. M.B. acknowledges the financial support of RAS, project NAMEFOAMS, CUP F72F-16003180002. L.C. acknowledges the financial support from the ERC AdG Ideas 2013 INSTABILITIES no. 340561, and from SteelPro project (financed by Regione Lombardia). D.M. acknowledges the financial support from National Group of Mathematical Physics (GNFM-INdAM).
Acknowledgements. The authors thank the 'Instabilities Lab' of the University of Trento.

References

1. Dong J, Fu L, Liu Q, Shen Z. 2018 Measuring and analyzing thermal deformations of the primary reflector of the Tianma radio telescope. *Exp. Astron.* **45**, 397–410. (doi:10.1007/s10686-018-9592-3)
2. Pisanu T. 2016 Metrology at the Sardinian Radio Telescope Metrology and Control of Large Telescopes, Green Bank, West Virginia, USA.
3. Giaccu GF, Corda S, Pisanu T, Buffa F, Brun M. 2016 Sardinian radio telescope: wind-induced pointing errors and surface deformations (preliminary results). Metrology and Control of Large Telescopes, Green Bank, West Virginia, USA.
4. Buffa F, Causin A, Cazzani A, Poppi S, Sanna G, Solci M, Stochino F, Turco E. 2017 The Sardinia Radio Telescope: a comparison between close-range photogrammetry and finite element models. *Mathematics and Mechanics of Solids* **22**, 1005–1026. (doi:10.1177/1081286515616227)
5. Boatti E, Vasios N, Bertoldi K. 2017 Origami metamaterials for tunable thermal expansion. *Adv. Mater.* **29**, 1700360. (doi:10.1002/adma.201700360)
6. Zhang Q, Wang W, Zhang J, Zhu X, Fu L. 2018 Thermally induced bending of ReS_2 nanowalls. *Adv. Mater.* **30**, 1704585. (doi:10.1002/adma.201704585)
7. Guo J, Wang J, Zeng S, Silberschmidt VV, Shen Y. 2017 Effects of the manufacturing process on the reliability of the multilayer structure in metalmumps actuators: residual stresses and variation of design parameters. *Micromachines* **8**, 348. (doi:10.3390/mi8120348)
8. Mary TA, Evans JSO, Vogt T, Sleight AW. 1996 Negative thermal expansion from 0.3 to 1050 Kelvin in ZrW_2O_8. *Science* **272**, 90–92. (doi:10.1126/science.272.5258.90)
9. Martinek C, Hummel FA. 1968 Linear thermal expansion of three tungstates. *J. Am. Ceram. Soc.* **51**, 227–228. (doi:10.1111/j.1151-2916.1968.tb11881.x)
10. Evans JSO. 1999 Negative thermal expansion materials. *J. Chem. Soc. Dalton* **19**, 3317–3326. (doi:10.1039/a904297k)
11. Schultz PC, Smyth HT, Douglas R, Ellis B (eds). 1970 Ultra-low-expansion glasses and their structure in the SiO_2 TiO_2 system. In *Amorphous materials*, pp. 453–164. New York, NY: Wiley-Interscience.
12. Kagaya HM, Soma T. 1993 Compression effect on specific heat and thermal expansion of Si and Ge. *Solid State Commun.* **85**, 617–621. (doi:10.1016/0038-1098(93)90320-M)
13. Lakes RS. 1996 Cellular solid structures with unbounded thermal expansion. *J. Mater. Sci. Lett.* **15**, 475–477. (doi:10.1007/BF00275406)
14. Lehman J, Lakes RS. 2013 Stiff, strong zero thermal expansion lattices via the Poisson effect. *J. Mater. Res.* **28**, 2499–2508. (doi:10.1557/jmr.2013.154)
15. Lakes RS. 2007 Solids with tunable positive or negative thermal expansion of bounded magnitude. *Appl. Phys. Lett.* **90**, 221905. (doi:10.1063/1.2743951)
16. Grima JN, Farrugia PS, Gatt R, Zammit V. 2007 A system with adjustable positive or negative thermal expansion. *Proc. R. Soc. A* **463**, 20071841. (doi:10.1098/rspa.2007.1841)
17. Miller W, Mackenzie DS, Smith CW, Evans KE. 2008 A generalized scale-independent mechanism for tailoring of thermal expansivity: positive and negative. *Mech. Mater.* **40**, 351–361. (doi:10.1016/j.mechmat.2007.09.004)
18. Sigmund O, Torquato T. 1996 Composites with extremal thermal expansion coefficients. *Appl. Phys. Lett.* **69**, 3203–3205. (doi:10.1063/1.117961)
19. Lim TC. 2012 Negative thermal expansion structures constructed from positive thermal expansion trusses. *J. Mater. Sci.* **47**, 368–373. (doi:10.1007/s10853-011-5806-z)
20. Palumbo NMA. 2011 Near-zero thermal expansivity 2-D lattice structures: Performance in terms of mass and mechanical properties. *Acta Mater.* **59**, 2392–2403. (doi:10.1016/j.actamat.2010.12.037)
21. Patterson K, Pellegrino S. 2014 Ultralightweight deformable mirrors. *Appl. Optics* **52**, 5327–5341. (doi:10.1364/AO.52.005327)

22. Yamamoto N, Gdoutos E, Toda R, White V, Manohara H, Daraio C. 2014 Thin films with ultralow thermal expansion. *Adv. Mater.* **26**, 3076–3080. (doi:10.1002/adma.201304997)
23. Grima JN, Oliveri L, Ellul B, Gatt R, Attard D, Cicala G, Recca G. 2010 Adjustable and negative thermal expansion from multilayered systems. *Phys. Status Solidi B* **4**, 133–135. (doi:10.1002/pssr.201004076)
24. Lim TC. 2001 Coefficient of thermal expansion of stacked auxetic and negative thermal expansion laminates. *Phys. Status Solidi B* **248**, 140–147. (doi:10.1002/pssb.200983970)
25. Kelly A, Stearn RJ, McCartney LN. 2006 Composite materials of controlled thermal expansion. *Compos. Sci. Technol.* **66**, 154–159. (doi:10.1016/j.compscitech.2005.04.025)
26. Grima JN, Ellul B, Attard D, Gatt R, Attard M. 2010 Composites with needlelike inclusions exhibiting negative thermal expansion: a preliminary investigation. *Compos. Sci. Technol.* **70**, 2248–2252. (doi:10.1016/j.compscitech.2010.05.003)
27. Grima JN, Farrugia PS, Gatt R, Zammit V. 2007 Connected triangles exhibiting negative Poisson's ratios and negative thermal expansion. *J. Phys. Soc. Jpn* **76**, 025001. (doi:10.1143/JPSJ.76.025001)
28. Wei K, Peng Y, Qu Z, Pei Y, Fang D. 2018 A cellular metastructure incorporating coupled negative thermal expansion and negative Poisson's ratio. *Int. J. Solids Struct.* **150**, 255–267. (doi:10.1016/j.ijsolstr.2018.06.018)
29. Huang CW, Chen L. 2016 Negative Poisson's ratio in modern functional materials. *Adv. Mater.* **28**, 8079–8096. (doi:10.1002/adma.201601363)
30. Cabras L, Brun M. 2014 Auxetic two-dimensional lattices with Poisson's ratio arbitrarily close to −1. *Proc. R. Soc. A* **470**, 2014538. (doi:10.1098/rspa.2014.0538)